JOURNAL OF SPACECRAFT AND ROCKETS
Vol. 29, No. 1, January–February 1992

Flow over an All-Body Hypersonic Aircraft: Experiment and Computation

William K. Lockman* and Scott L. Lawrence†
NASA Ames Research Center, Moffett Field, California 94035
and
Joseph W. Cleary‡
Eloret Institute, Sunnyvale, California 94087

The objective of the present investigation is to establish a benchmark experimental data base for a generic hypersonic vehicle shape for validation and/or calibration of advanced computational fluid dynamics computer codes. This paper includes results from the comprehensive test program conducted in the NASA Ames 3.5-ft Hypersonic Wind Tunnel for a generic all-body hypersonic aircraft model. Experimental and computational results on flow visualization, surface pressures, surface convective heat transfer, and pitot-pressure flowfield surveys are presented. Comparisons of the experimental results with computational results from an upwind parabolized Navier-Stokes code developed at NASA Ames demonstrate the capabilities of this code.

Introduction

THE advanced computational fluid dynamics (CFD) computer codes being developed for use in the design of such hypersonic aircraft as the National Aero-Space Plane (NASP) and other hypersonic vehicles require comparisons of the computational results with a broad spectrum of experimental data to fully assess the validity of the codes and to develop confidence in the numerical simulation procedures. This is particularly true for complex flowfields with such features as boundary-layer transition and turbulence, rapid flow expansions, and leeside flow with the attendant flow separation and vortices. Validated codes for such flowfields will be critical to the development of the NASP and other hypersonic vehicles. Therefore, the objective of the present investigation is to establish a benchmark experimental data base for a generic hypersonic vehicle shape for validation and/or calibration of advanced CFD computer codes. This is being done by conducting a comprehensive test program for a generic all-body hypersonic aircraft model in the NASA Ames 3.5-ft Hypersonic Wind Tunnel to obtain pertinent surface and flowfield data over a broad range of test conditions. Experimental and computational results on flow visualization, surface pressures, surface convective heat transfer, and pitot-pressure flowfield surveys will be presented in this paper. Of particular significance, comparisons of the experimental results with computational results from the NASA Ames UPS code (an upwind parabolized Navier-Stokes solver) will be shown to demonstrate the capabilities of this code. Some comparisons of the data with computations from approximate inviscid methods will also be given.

Experimental Methods

Facility

The NASA Ames 3.5-ft Hypersonic Wind Tunnel (HWT) is a closed-circuit, blow-down-type tunnel with a pebble-bed heater to heat the air to prevent liquefaction and with interchangeable, axisymmetric contoured nozzles to achieve the test Mach numbers of 5, 7, and 10.[1] The test section is an open-jet type enclosed within a chamber approximately 3.7 m (12 ft) in diameter and 12 m (40 ft) in length, arranged transversely to the flow direction. Within this chamber is a model quick-insert mechanism for quickly moving models (transit time as short as ½ s) into and out of the airstream. This is particularly important for heat transfer studies where the model is isothermal prior to insertion into the flow and the transit time through the tunnel boundary layer has an insignificant effect on the heating measurements. All optics for flow-visualization studies are also enclosed within the chamber, thus eliminating the need for viewing through any windows.

Model

The all-body hypersonic aircraft model is representative of a hypersonic cruise vehicle derived from analytical studies.[2-5] The aerodynamic force and moment characteristics of this configuration were previously investigated from subsonic to hypersonic Mach numbers.[6] The basic all-body model (without control surfaces) is shown in Figs. 1 and 2. Figure 1 is a sketch of the model to show the basic model geometry and dimensions; Fig. 2 is a photograph of the model installed in the NASA Ames 3.5-ft HWT. The support sting for mounting the model in the tunnel is attached to the model along the afterbody centerline (see Fig. 2). The model has a delta planform with leading-edge sweepback of 75 deg and total axial length L of 0.9144 m (3 ft). The present model is larger than the force model (L = 0.4826 m) of Ref. 6. The forebody is an elliptic cone with a major-to-minor axis ratio of 4, and the afterbody

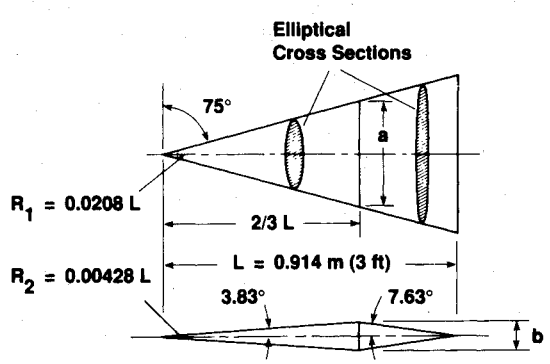

Fig. 1 All-body model without control surfaces.

Presented as Paper 90-3067 at the AIAA 8th Applied Aerodynamics Conference, Portland, OR, Aug. 20–22, 1990; received Feb. 8, 1991; revision received June 21, 1991; accepted for publication July 29, 1991.

*Research Scientist, Aerothermodynamics Branch. Member AIAA.
†Research Scientist, Applied Computational Fluids Branch. Member AIAA.
‡Research Scientist. Member AIAA.

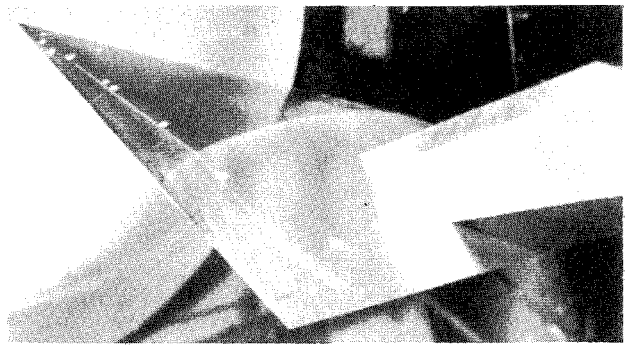

Fig. 2 All-body model without control surfaces in NASA Ames 3.5-ft Hypersonic Wind Tunnel.

has elliptical cross sections with a sharp straight-line trailing edge. The juncture between the forebody and afterbody occurs at two-thirds of the body length. The model nose can be either sharp or blunt with the blunt nose blended smoothly into the elliptical shape of the body. Only results for the sharp-nosed model will be given in this paper. The model has only been tested to date without control surfaces (combination horizontal/vertical tails). This relatively simple model geometry can be gridded easily for CFD codes.

Test Conditions

The test conditions for this study include nominal freestream Mach numbers M_∞ of 5, 7, and 10; freestream Reynolds numbers $Re_{\infty,L}$, based on model length of 0.9144 m (3 ft), from 1.5×10^6 to 25×10^6 (laminar to turbulent flows); and model angles of attack α of 0, 5, 10, and 15 deg (attached and separated flows). For computing the tunnel flow conditions, the air is treated as a thermally perfect, calorically imperfect gas with the relatively small imperfect-gas effects accounted for by the analysis of Ref. 7. Keyes' equation[8] for viscosity, rather than Sutherland's equation,[7] is used because of the low freestream static temperatures (approximately 50 K). Boundary-layer transition studies using heat transfer measurements were conducted to assess the state of the boundary layer (laminar, transitional, or turbulent) for the specific test conditions of this experiment.

Results will be given in the present paper for $M_\infty = 7.4$ and $Re_{\infty,L} = 5 \times 10^6$ to 25×10^6. These conditions were for a nominal freestream total temperature T_t of 722 K (1300°R) with a freestream static temperature T_∞ of 62 K (111°R) and a model wall temperature T_w of 300 K (540°R). The ratio of the wall enthalpy H_w to the freestream total enthalpy H_t is $H_w/H_t = 0.4$. The values for M_∞, $Re_{\infty,L}$, T_∞, and T_w were used for the UPS code computations, along with the viscosity from Keyes' equation.

Measurements

Flow-visualization data (shadowgraphs and surface oil-flow patterns), surface pressures, surface convective heat transfer, and pitot-pressure flowfield surveys will be presented in the paper for the basic all-body model without control surfaces.

The skin-friction lines (limiting streamlines) were visualized using the surface oil-flow technique.[9] The model was painted with a thin layer of high-temperature, flat-black paint; wet sanded; and then coated with a white oil mixture (vacuum pump oil, titanium dioxide powder, and oleic acid) to provide good contrast for photographs. The model was exposed to the tunnel flow for approximately 10–30 s, depending on test conditions, to develop a stable oil-flow pattern. During the runs, observations of the model with a video camera demonstrated that the model travel through the tunnel free-jet shear layer during the model insertion and retraction had no adverse effects on the flow patterns developed during the runs. Postrun still photographs were made of the surface oil-flow patterns.

The model has 192 surface pressure taps (1-mm orifice diameter) connected to electronic pressure scanners installed inside the model for measurements. The pressure transducers measured differential pressure with a vacuum reference. To insure greater measurement accuracy, all pressure transducers were calibrated immediately before each run.

To provide surface heat transfer measurements using the thin-skin technique,[10] a new thin-wall (0.5-mm-thick) 17-4PH stainless steel cover plate with 62 chromel-constantan thermocouples spot welded at selected locations (from 25 to 85% of model length and to 70% of model semispan) was built to replace the existing top cover plate for the pressure model. The model is tested at $\pm\alpha$ to obtain leeward and windward heating data, respectively. The presence of the model support sting limited the number of measurement locations for the afterbody.

For pitot-pressure surveys, two rakes are used with one mounted on the model centerline and the other at selected outboard stations. The rakes can be positioned fore and aft at various x/L stations along the lower surface. The model is tested at $\pm\alpha$ to obtain windward and leeward surveys, respectively. The probes on both rakes are stainless steel tubing with an outside diameter of 1 mm and an inside diameter of 0.8 mm. The ends of the probes on the centerline rake were flattened to allow closer probe spacing near the wall.

Computational Methods

Comparisons of the experimental results with computational results from UPS code developed at NASA Ames and some approximate inviscid methods will be presented later.

The UPS code[11] uses an upwind method for solving the parabolized Navier-Stokes (PNS) equations. The code employs a numerical algorithm that is second-order accurate and upwind in the crossflow directions. The improved shock-capturing characteristics of the algorithm are due in large part to the upwinding. Presently, the algorithm is first-order accurate in the streamwise direction. This is generally considered sufficient accuracy for noniterative space-marching methods because step sizes are restricted much more by stability constraints than by accuracy considerations. The algorithm is implicit both in the interior of the flowfield and in the treatment of the boundaries. Freestream conditions are imposed at the outer boundary and all shocks are captured rather than fitted. Finally, the method makes use of the finite volume approach to ensure that fluxes are treated in a conservative manner. The dissipation of upwind methods allows shock waves to be sharply captured without introducing the oscillations that are typically obtained using conventional central-differencing schemes. Also, because the dissipation is inherent within the algorithm, it is not necessary for the user to specify the values of smoothing parameters. Presently, there is capability for modeling either laminar or turbulent flow of a perfect gas (used for this study), equilibrium air, or nonequilibrium air. The onset of transition can be specified either as a streamwise station or as a local value of Re_θ/M_e, where Re_θ is the local Reynolds number based on momentum thickness and M_e is the local Mach number at the boundary-layer edge. For all of the UPS results presented here, transition was assumed to begin at $x/L = 0.05$ and end at $x/L = 0.1$. The algebraic eddy viscosity turbulence model of Baldwin and Lomax[12] is presently used with modifications suggested by Degani and Schiff[13] for treatment of crossflow separation. Air in chemical equilibrium is modeled using curve fits for the thermodynamic and transport properties.[14] In addition, a version of the code incorporating nonequilibrium air chemistry using a loosely coupled approach has been developed recently.[15]

The UPS results presented in the following section were computed using a grid containing 90 cells in each crossflow direction. Grid points were clustered near the wall with normal spacings to the first field point generally between 0.2×10^{-5} and 0.5×10^{-5} m. Values of y^+ (dimensionless distance from the wall in viscous wall units) to the first field point on the

windward centerline ranged from 0.2 to 0.5 at $\alpha = 15$ deg. Initial conditions for the sharp-nosed body were self-generated near the nose ($x/L = 0.05$) using an iterative procedure that produces a conically similar solution. From the conical starting solution, the calculations proceeded downstream using a marching step size of approximately 2 mm. The calculations were terminated at 90% of the body length because of grid-generation limitations. Total CPU time for the calculations was generally 10–15 min on a Cray Y-MP supercomputer.

The approximate inviscid methods include simple tangent-cone and tangent-wedge methods[16] for the windward surfaces, the infinite swept-cylinder method for the leading edge, and an approximation for conical-flow hodographs[17] for the windward flowfield. These simple methods are useful tools for providing estimates of the windward pressures.

Results and Discussion

Experimental and computational results on flow visualization, surface pressures, surface heat transfer, and pitot-pressure flowfield surveys will now be presented. Results will be given for the sharp-nosed model at $M_\infty = 7.4$ to illustrate the basic observations and conclusions from the investigation for the all-body model. Uncertainty intervals from an error analysis of the various experimental measurements are indicated as error bars on the corresponding data plots.

Flow Visualization

The windward bow shock, forebody boundary layer, and flow expansion at the juncture of the forebody and afterbody are visible in the shadowgraph in Fig. 3 for the vertical symmetry plane at $\alpha = 15$ deg.

Figure 4 is a graph at $M_\infty = 7.4$ of the forebody shock-wave angle Θ_w as a function of the lower-surface inclination angle Θ_s for the vertical symmetry plane of the sharp-nosed model. As shown on the model sketch, these angles are measured from the horizontal freestream flow direction. The value for Θ_s is the sum of the angle of attack α and the forebody half angle of 3.83 deg. Experimental values of Θ_w from shadowgraphs for $\alpha = 0$, 5, 10, and 15 deg ($\Theta_s = 3.83$, 8.83, 13.83, and 18.83 deg, respectively) are plotted. The angles of attack and shock angles were measured to within ± 0.3 deg. Also plotted are Θ_w values computed by the UPS code for turbulent flow at the same angles of attack. Shock location was defined to be at the location of the maximum density gradient in the captured shock. As might be expected, the UPS code results are in excellent agreement with the shock-wave data. In addition, estimates of Θ_w by simple tangent-cone and tangent-wedge inviscid methods are shown. Comparing the data and UPS code results to these approximate methods indicates a change from a wedge-like shock to a conical shock with increasing angle of attack (increasing Θ_s). Similar trends were observed for $M_\infty = 5.3$ and 10.3.

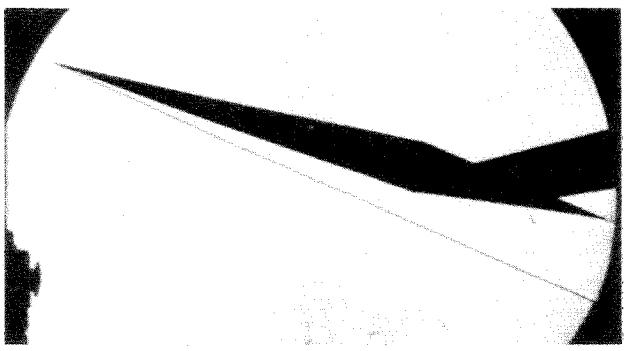

Fig. 3 Shadowgraph for vertical symmetry plane: $\alpha = 15$ deg; $M_\infty = 7.4$; $Re_{\infty,L} = 15 \times 10^6$; $H_w/H_t = 0.4$.

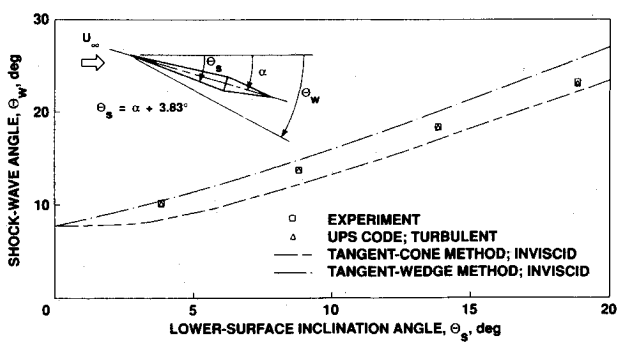

Fig. 4 Forebody shock-wave angle: $M_\infty = 7.4$, $Re_{\infty,L} = 15 \times 10^6$; $H_w/H_t = 0.4$.

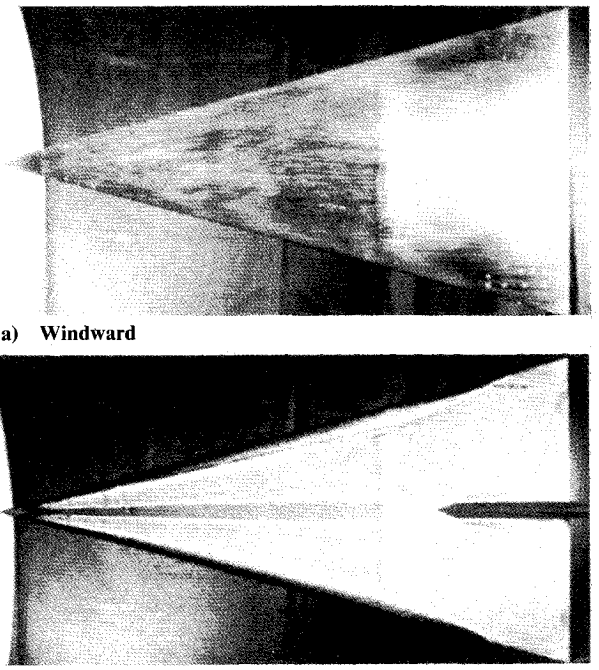

a) Windward

b) Leeward

Fig. 5 Surface oil-flow patterns: $\alpha = 15$ deg; $M_\infty = 7.4$, $Re_{\infty,L} = 15 \times 10^6$; $H_w/H_t = 0.4$.

Photographs of the oil-flow patterns for the windward and leeward surfaces at $\alpha = 15$ deg are shown in Fig. 5. As the angle of attack was increased for the sharp-nosed model, the windward oil-flow patterns changed from wedge-like (strip) at $\alpha = 0$ deg to conical surface flow patterns at higher angles of attack. The conical pattern of the skin-friction lines is visible on the windward surface of the model forebody at $\alpha = 15$ deg (Fig. 5a). However, the skin-friction lines begin to converge inward toward the model centerline at the forebody/afterbody juncture where the flow expands and becomes nonconical. These features were characteristic of the flows at all three Mach numbers for the sharp-nosed model.

The leeward oil-flow pattern at $\alpha = 15$ deg (Fig. 5b) illustrates the complex leeward vortical flows characteristic of conical and delta-planform bodies at angle of attack. The reattachment line for the two primary vortices is visible on the most leeward ray at the symmetry plane. The presence of two secondary vortices is also visible just outboard of the primary reattachment region. The actual crossflow separation lines for the primary vortices near the model leading edges are not definitive because the oil-flow pattern may not be fully developed with time in these regions. The slight disturbances in the oil-flow pattern near the nose tip are due to transverse joints in model surface. The two straight lines along conical rays, just inboard from each leading edge, are joints for the removable cover plate on leeward surface. The shock/boundary-layer interaction at the sting attachment on the afterbody can also be seen. No other significant details are apparent in the oil-flow pattern for the low-shear regions of the afterbody.

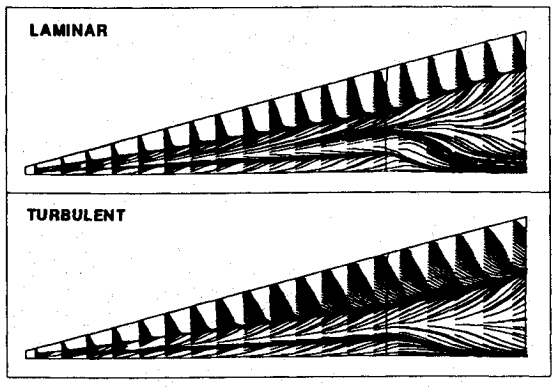

Fig. 6 Particle traces for leeward surface by UPS code (simulated surface oil-flow patterns; x/L = 0.0–0.9): α = 15 deg, M_∞ = 7.4; $Re_{\infty,L}$ = 15 × 10^6; H_w/H_t = 0.4.

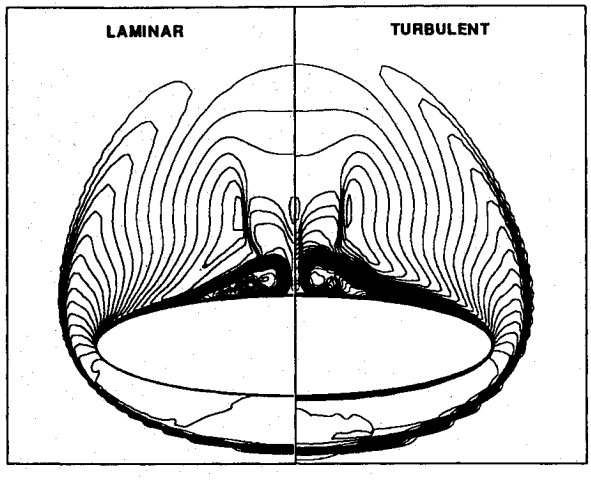

Fig. 7 Mach number contours for crossflow plane at x/L = 0.6 by UPS code: α = 15 deg; M_∞ = 7.4; $Re_{\infty,L}$ = 15 × 10^6; H_w/H_t = 0.4.

The particle traces on the leeward surface computed by the UPS code for α = 15 deg and M_∞ = 7.4 are shown in Fig. 6. Results are given for both laminar and turbulent flows. For each case, the right side of the model is shown with the symmetry plane at the bottom. The addition of turbulent viscosity is shown to cause a slight change in the computed leeward flowfield. Both cases indicate the presence of a secondary crossflow separation with the separation and reattachment lines between the primary separation and the symmetry plane. The reattachment line is closer to the symmetry plane for the turbulent case than for the laminar case, which is in better agreement with the experimental oil-flow pattern of Fig. 5b. The prediction of the secondary separation in the turbulent solution can be attributed to the implementation of the Degani-Schiff[13] modifications to the Baldwin-Lomax turbulence model.[12] Computations with the unaltered Baldwin-Lomax model suffered from the addition of excessive dissipation in the crossflow separation region and produced only a primary separation with reattachment at the plane of symmetry.

The Mach number contours in the crossflow plane at x/L = 0.6 computed by the UPS code for the same conditions as for the surface particle traces are shown in Fig. 7. Contours for laminar and turbulent flows are shown on the left and right sides, respectively, of the model centerline. The leeward Mach contours further illustrate the crossflow primary and secondary separations. The turbulent solution exhibits a much thicker windward boundary layer and the location of the primary separation is shown to be nearer the leeward centerline. A crossflow shock wave is clearly indicated in both solutions. Except for a slight alteration in the position of this shock, the turbulence model has essentially no effect on the inviscid portion of the flowfield. The outer-shock waviness is due to linear interpolation being used in the plotting routine and is typical of shocks that are captured within 2–3 grid points and not aligned with the grid. The amplitude and period of these waves are reduced as the grid is refined.

Surface Pressures

The effects of angle of attack on the windward and leeward centerline pressures are summarized in Fig. 8 for α = 0, 5, 10, and 15 deg. Also shown are predictions of the pressures by the UPS code for turbulent flow. The surface pressure ratio (ratio of surface pressure p to freestream static pressure p_∞) is plotted vs the axial station x/L along the surface centerline for the vertical symmetry plane. The increasing windward and decreasing leeward pressures with increasing angle of attack and the drop in pressure at the forebody/afterbody juncture (x/L = ⅔) are readily seen. There is generally good agreement between the windward pressures by the experiment and by the UPS code, with greater differences at the higher angles of attack where the forebody pressures are underpredicted. The agreement between the leeward pressures by the experiment and by the UPS code is quite good, considering the relatively low pressures and the complexity of the leeward flowfield.

The surface pressure ratios along the leading edge at α = 0 deg are plotted in Fig. 9. Experimental values are shown for

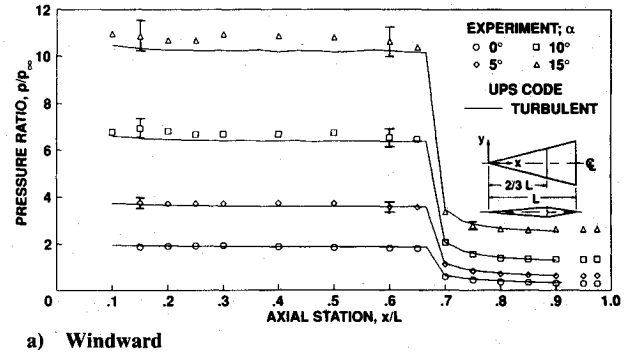

a) Windward

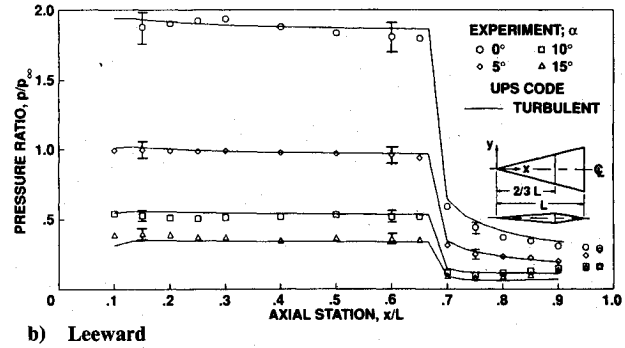

b) Leeward

Fig. 8 Effect of angle of attack on centerline surface pressures: M_∞ = 7.4; $Re_{\infty,L}$ = 15 × 10^6; H_w/H_t = 0.4.

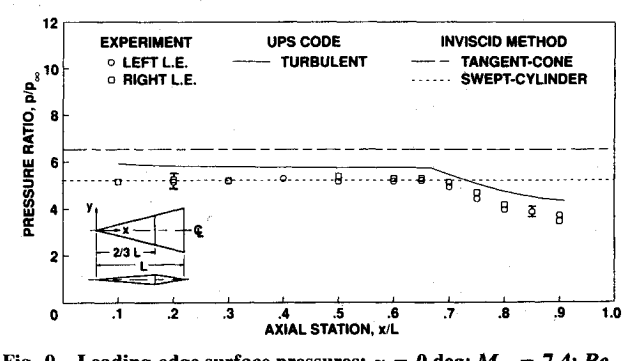

Fig. 9 Leading-edge surface pressures: α = 0 deg; M_∞ = 7.4; $Re_{\infty,L}$ = 15 × 10^6; H_w/H_t = 0.4.

both the left and right leading edges, which show relatively small differences in the data considering the difficulty of measuring these pressures with the large pressure gradient at the leading edge. Of particular interest are the relatively constant pressures along the conical forebody followed by the decreasing pressures along the nonconical afterbody. The afterbody has some relieving effect on the leading-edge flow because of the decreasing afterbody thickness with increasing x/L. The infinite swept-cylinder method gives a good estimate of the leading-edge pressure for the forebody, whereas the tangent-cone method overestimates the forebody leading-edge pressures. None of these simple methods correctly estimate the afterbody pressures because they do not account for the changing afterbody geometry. The UPS code results for turbulent flow somewhat overpredict the leading-edge pressure data, but show the correct trend for the afterbody.

The spanwise surface-pressure distributions for the forebody and afterbody stations of $x/L = 0.6$ and 0.8, respectively, at $\alpha = 0$ deg are now given in Fig. 10. The pressure ratio p/p_∞ is plotted vs y/y_{LE} for the two x/L values, where y is the spanwise coordinate and y_{LE} is the value of y at the leading edge for the given x/L station. Since the pressure taps were primarily on the left (port) side of the model, the results are plotted for negative y. It should be noted that the data at a

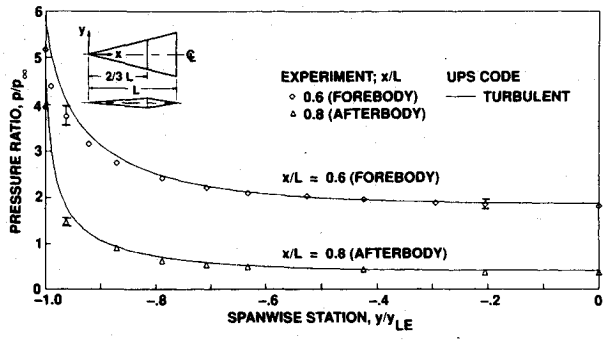

Fig. 10 Spanwise surface-pressure distributions for forebody and afterbody: $\alpha = 0$ deg; $M_\infty = 7.4$; $Re_{\infty,L} = 15 \times 10^6$; $H_w/H_t = 0.4$.

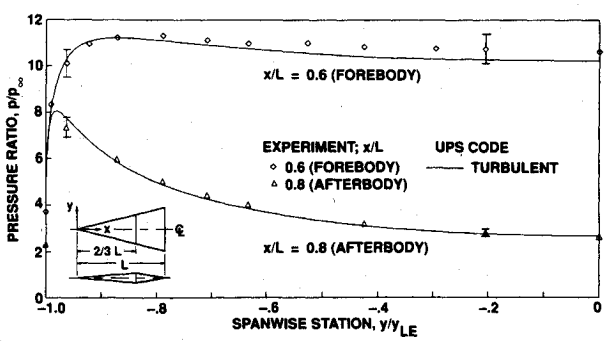

a) Windward

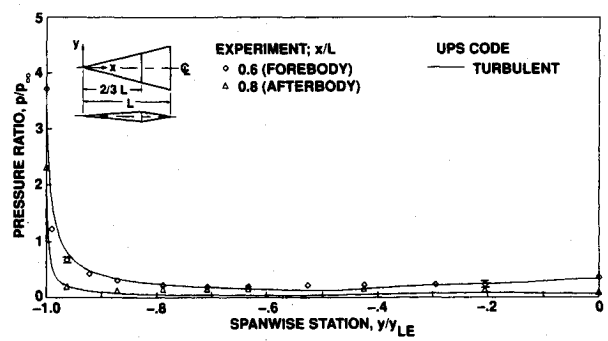

b) Leeward

Fig. 11 Spanwise surface-pressure distributions for forebody and afterbody: $\alpha = 15$ deg; $M_\infty = 7.4$; $Re_{\infty,L} = 15 \times 10^6$; $H_w/H_t = 0.4$.

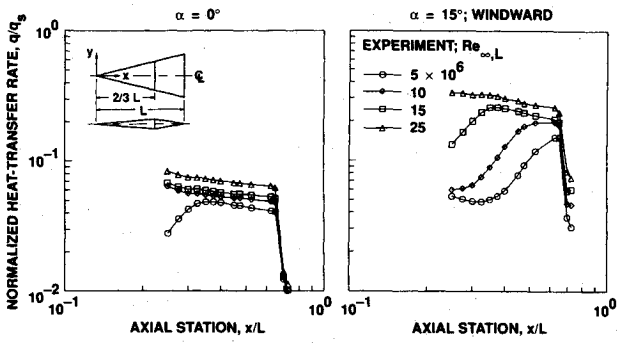

q_s = Stagnation-point heat-transfer rate for reference sphere (R = 0.01L)

Fig. 12 Effect of Reynolds number on centerline heat transfer: $M_\infty = 7.4$; $H_w/H_t = 0.4$.

given y/y_{LE} value for various x/L values are along a conical ray from the nose tip in the planform view of model. The difference in pressure levels between the forebody and afterbody is readily seen from the figure. The UPS code results are in good agreement with the corresponding experimental data for these two stations except for predictions of pressures higher than the experimental values approaching the leading edge. Although not presented here, the experimental and computational pressures at a given y/y_{LE} are essentially invariant with x/L for the forebody, thus indicating the conical forebody flow, but decrease with increasing x/L for the afterbody, thus indicating the nonconical afterbody flow.

The spanwise surface-pressure distributions for the windward forebody and afterbody stations of $x/L = 0.6$ and 0.8, respectively, at $\alpha = 15$ deg are now plotted in Fig. 11a to illustrate the differences between the forebody and afterbody pressures and to show the comparisons with UPS code computations for these two stations at angle of attack. The differences in pressure levels and distributions between the forebody and afterbody are readily seen from the figure. By comparing this plot with Fig. 10 at $\alpha = 0$ deg, the changes in the pressure distributions from the forebody to the afterbody at $\alpha = 15$ deg are even more pronounced than at $\alpha = 0$ deg. The agreement between the experimental and UPS code results are seen to be good except approaching the forebody centerline where, as was previously shown in Fig. 8a, the UPS code underpredicts the windward pressures.

The spanwise pressure distributions for the leeward forebody and afterbody stations of $x/L = 0.6$ and 0.8, respectively, at $\alpha = 15$ deg are now plotted in Fig. 11b to illustrate the differences between the forebody and afterbody pressures and to show the comparisons with UPS code computations for these two stations at angle of attack. The forebody/afterbody differences in these relatively small leeward pressure levels are apparent. The agreement between the experimental and UPS code results are seen to be good except near midspan and approaching the leading edge.

Although not presented here, as for $\alpha = 0$ deg, the pressures for $\alpha = 15$ deg at a given y/y_{LE} are essentially invariant with x/L for the forebody, thus indicating the conical forebody flow, but decrease with increasing x/L for the afterbody, thus indicating the nonconical afterbody flow.

Surface Heat Transfer

The effects of both Reynolds number and angle of attack on the experimental heat transfer along the all-body centerline for the vertical symmetry plane are shown in Fig. 12 for $\alpha = 0$ and 15 deg (windward surface). Log-log plots of the normalized heat transfer rate (ratio of surface heat transfer rate q to a computed heat transfer rate q_s for a reference sphere [$R = 0.01L$] by the method of Fay and Riddell[18]) vs the axial station x/L are shown. At a fixed value of $Re_{\infty,L}$ on such a log-log plot, the heating rate should vary linearly and inversely with increasing x/L for the portions of the conical forebody flow

with a laminar or turbulent boundary layer. Only experimental results are shown for the sharp-nosed model at freestream Reynolds numbers $Re_{\infty,L}$ from 5×10^6 to 25×10^6. The data are presented as q/q_s vs x/L to readily show the forward movement of boundary-layer transition onset with increased $Re_{\infty,L}$ for either angle of attack and the rearward movement with increased angle of attack for a fixed value of $Re_{\infty,L}$. Also, the large decrease in heating at the forebody/afterbody juncture ($x/L = \frac{2}{3}$) is quite evident with the heating further decreasing along the afterbody. The afterbody heating is almost an order of magnitude lower than the turbulent forebody heating. As previously mentioned, the afterbody data

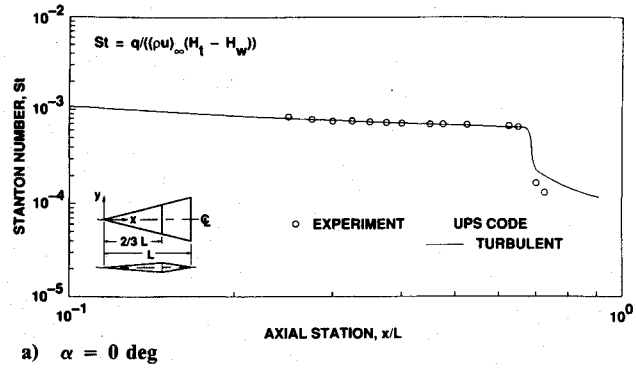

a) $\alpha = 0$ deg

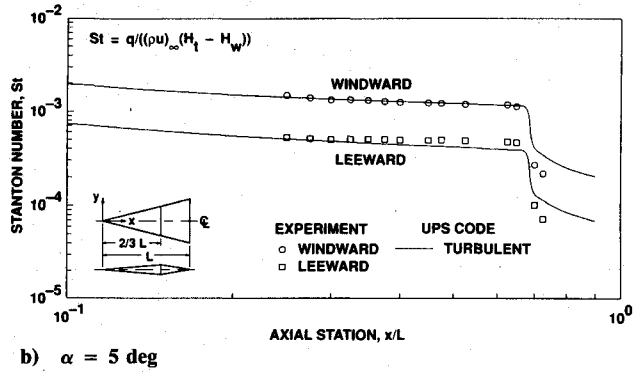

b) $\alpha = 5$ deg

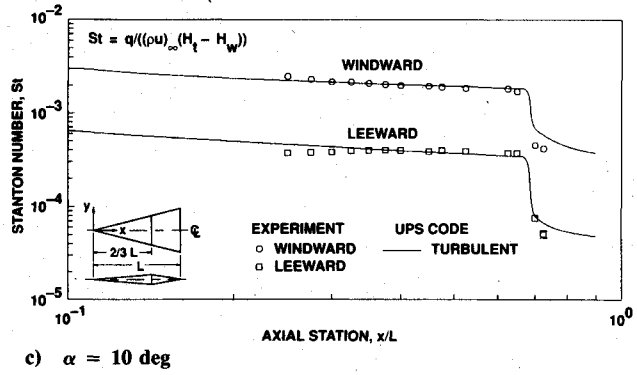

c) $\alpha = 10$ deg

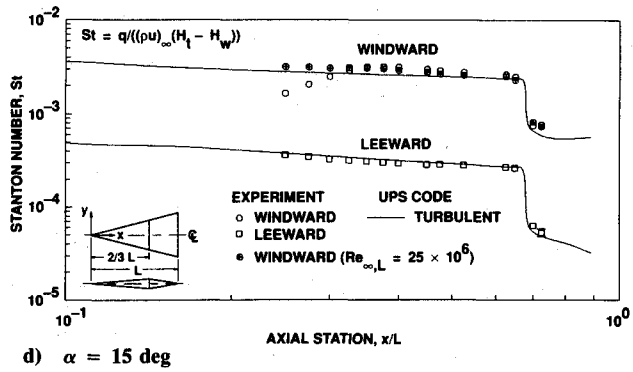

d) $\alpha = 15$ deg

Fig. 13 Centerline heat transfer distributions for various angles of attack: $M_\infty = 7.4$; $Re_{\infty,L} = 15 \times 10^6$; $H_w/H_t = 0.4$.

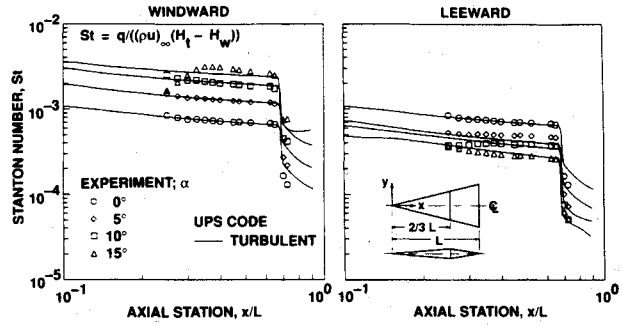

Fig. 14 Effect of angle of attack on centerline heat transfer: $M_\infty = 7.4$; $Re_{\infty,L} = 15 \times 10^6$; $H_w/H_t = 0.4$.

are limited because of the presence of the sting along the surface centerline.

Comparisons of the experimental and UPS code results for the surface heat transfer distributions along the centerline are given in Fig. 13 at $\alpha = 0$, 5, 10, and 15 deg for $M_\infty = 7.4$ and $Re_{\infty,L} = 15 \times 10^6$. The Stanton number St $\{St = q/[(\rho u)_\infty (H_t - H_w)]\}$ used for the comparisons is based on the surface heat transfer rate q, freestream unit mass flow $(\rho u)_\infty$, freestream total enthalpy H_t, and wall enthalpy H_w. For this figure, the Stanton number is plotted on log-log plots vs axial station x/L along the surface centerline for the vertical symmetry plane. On such log-log plots, the Stanton number should vary linearly and inversely with increasing x/L for the portions of the conical forebody flow with a laminar or turbulent boundary layer. The experimental data and the UPS code results indicate this to be the case for the turbulent forebody flows at the angles of attack and Reynolds numbers given here. The large differences in heating levels between the windward and leeward sides for a given angle of attack and the increasing windward and decreasing leeward heating with increasing angle of attack are readily seen.

The windward heating for the forebody at $\alpha = 0$–10 deg is predicted quite well by the UPS code. There are minor differences between the experimental and UPS code results for the leeward forebody, where oil-flow studies illustrate the complex leeward flow with vortices at angle of attack. The afterbody heating is overpredicted by the UPS code for both the windward and leeward centerlines at these test conditions.

At $\alpha = 15$ deg, the experimental heating results in Fig. 12 for the windward centerline indicated that the forebody boundary layer was transitional for $Re_{\infty,L} = 15 \times 10^6$ and turbulent for $Re_{\infty,L} = 25 \times 10^6$ in the x/L range of the heating measurements. Thus, in Fig. 13d, the experimental windward heating for the forebody at $Re_{\infty,L} = 15 \times 10^6$ overshoots the UPS code turbulent heating results for the same $Re_{\infty,L}$, as is characteristic for transitional heating. Also shown are the experimental heating data for $Re_{\infty,L} = 25 \times 10^6$, which are comparable to the windward levels predicted by the UPS code for $Re_{\infty,L} = 15 \times 10^6$. There is good agreement between the experimental and UPS code results for the leeward forebody at $\alpha = 15$ deg. For this angle of attack and these test conditions, the afterbody heating is underpredicted by the turbulent UPS code for both the windward and leeward sides, as opposed to the overprediction for the lower angles of attack.

Summary plots showing the effects of angle-of-attack variation on both the windward and leeward heating for the same freestream Reynolds number of 15×10^6 are given in Fig. 14. The increasing windward and decreasing leeward heating with increasing angle of attack are readily seen. Both plots have the same scale to readily show the large differences in heating levels between the windward and leeward sides for the corresponding angles of attack.

The spanwise heat transfer distributions for the forebody are shown in Figs. 15 for $\alpha = 0$, 5, 10, and 15 deg. The Stanton number St is plotted vs y/y_{LE} for $x/L = 0.5$ and 0.6. It should again be noted that the data at a given y/y_{LE} value for

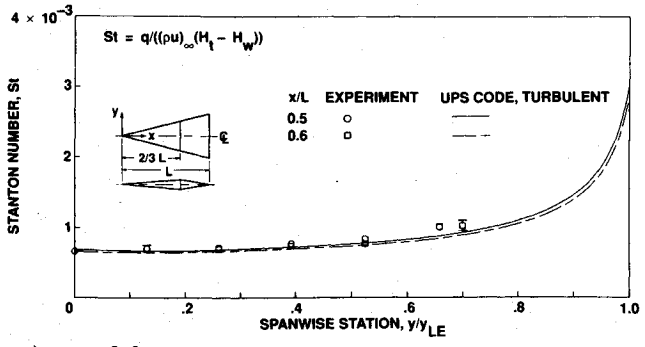

a) α = 0 deg

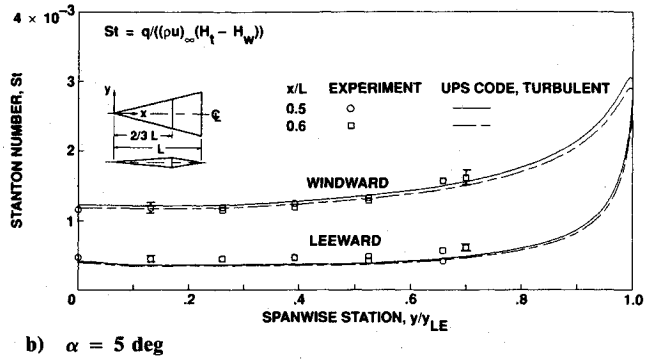

b) α = 5 deg

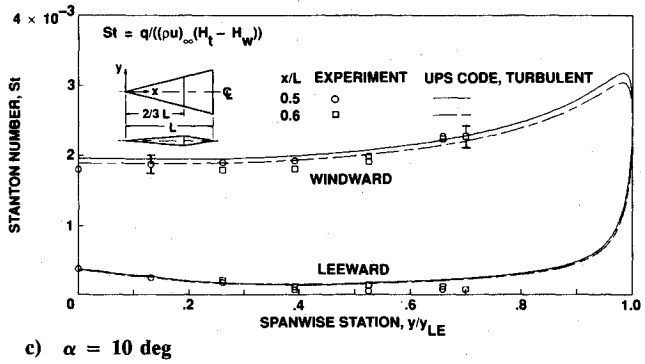

c) α = 10 deg

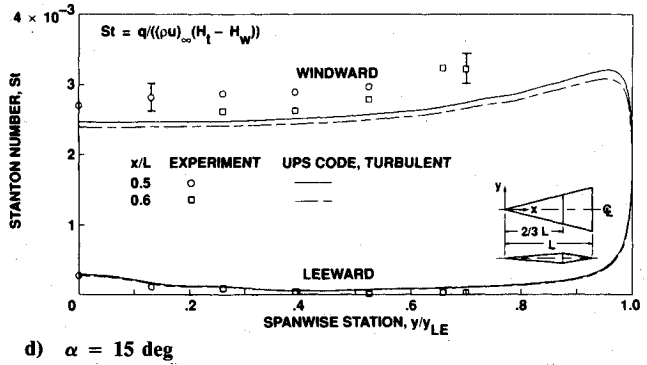

d) α = 15 deg

Fig. 15 Spanwise heat transfer distributions for forebody: M_∞ = 7.4; $Re_{\infty,L}$ = 15 × 10⁶; H_w/H_t = 0.4.

various x/L values are along a conical ray from the nose tip in the planform view of the model. Linear plots are used to directly illustrate the spanwise variation in heating, differences between heating values for the two x/L stations, and differences between the experimental and UPS code results. As previously mentioned, the spanwise heating measurements were limited to $y/y_{LE} \leq 0.7$ for this study.

In Fig. 15a for α = 0 deg, a spanwise increase in heating from the model centerline toward the leading edge is shown with relatively small decreases in heating between x/L stations along a conical ray at any given value of y/y_{LE}. There is good agreement between the experimental and UPS code results for the limited range of the measurements.

For α = 5 and 10 deg (Figs. 15b and 15c, respectively), the heating generally increases spanwise toward the leading edge for both the windward and leeward sides, with a local maximum on the leeward centerline where oil-flow studies and UPS code solutions showed reattachment of two vortices at angle of attack. As was previously shown for α = 0 deg, there are relatively small differences between the results at the two x/L stations for both the windward and leeward sides. The agreement between the experimental and UPS code results is generally good, with greater percentage differences for the leeward side.

Since the windward boundary-layer flow for α = 15 deg at $Re_{\infty,L}$ = 15 × 10⁶ was previously shown to be transitional ahead of x/L = 0.5 (Fig. 12), the experimental spanwise heating data for not fully developed turbulent flow at x/L = 0.5 and 0.6 (Fig. 15d) are not predicted well by the UPS code, which assumed a fully developed turbulent flow on the windward side. As would be expected and was shown for the centerline, the experimental spanwise heating data near the end of transition exceed the levels predicted for turbulent flow by the UPS code. However, the UPS code predicts the general spanwise trends for the leeward side, with local maxima on and just off the centerline. Greater percentage differences are observed outboard. Considering the relatively low leeward heating levels and the complexity of the leeward flow with primary and secondary vortices, the apparent agreement between experiment and the UPS code is noteworthy.

Pitot-Pressure Surveys

The purpose of Fig. 16 is to show the basic features of the shock-layer flow on the afterbody lower surface at the rake survey station. Experimental data for α = 0 and 15 deg are compared with a simplified inviscid model of the flow. Pitot pressure (normalized by freestream pitot pressure) is plotted vs distance from the model surface (normalized by model length). This distance is measured perpendicular to the horizontal symmetry plane of the model (see model sketch on figure). The pitot-pressure profiles consist of an outer conical-flow region at the shock wave, a central flow-expansion region, and an inner viscous flow region adjacent to the wall. The inviscid flow model consists of the outer conical-flow region at the shock wave, the central region represented by a Prandtl-Meyer expansion, and a two-dimensional planar region near the surface where the flow turns parallel to the surface. To construct the inviscid model, the forebody surface Mach number must be known for calculation of the Prandtl-Meyer expansion. Using the experimental shock-wave angle, an approximation for conical-flow hodographs[17] was used to calculate the forebody Mach number. The forebody and afterbody local Mach numbers were estimated to be 6.70 and 9.45, respectively, for α = 0 deg, and 4.25 and 5.40, respectively, for α = 15 deg. These values are based on M_∞ = 7.43. As shown in the figure, the main features of the inviscid model agree reasonably well with experiment except near the surface where viscous effects predominate.

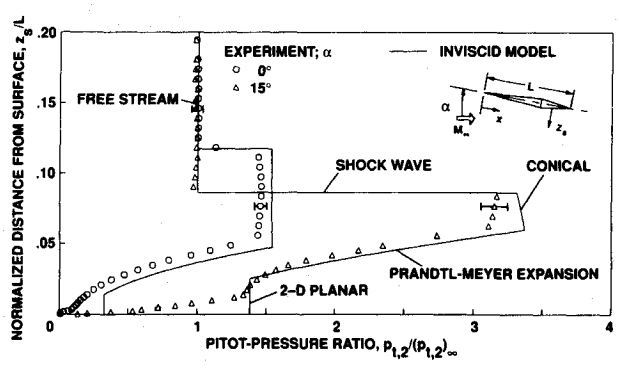

Fig. 16 Comparison of experimental pitot-pressure distributions with inviscid model of flow: afterbody centerline x/L = 0.8; M_∞ = 7.4; $Re_{\infty,L}$ = 15 × 10⁶; H_w/H_t = 0.4.

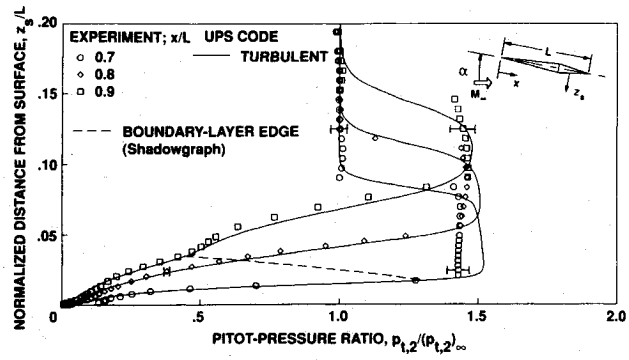

a) Entire shock layer

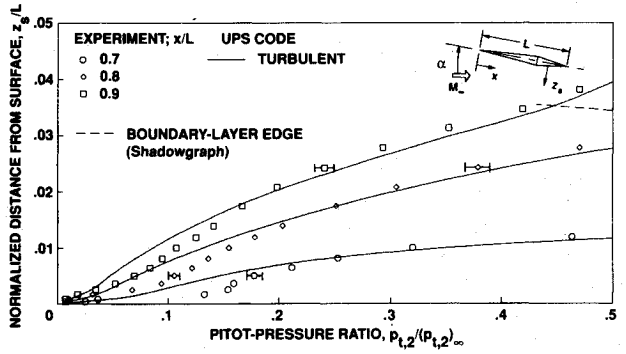

b) Near wall

Fig. 17 Pitot-pressure distributions at various afterbody stations for model centerline: $\alpha = 0$ deg; $M_\infty = 7.4$; $Re_{\infty,L} = 15 \times 10^6$; $H_w/H_t = 0.4$.

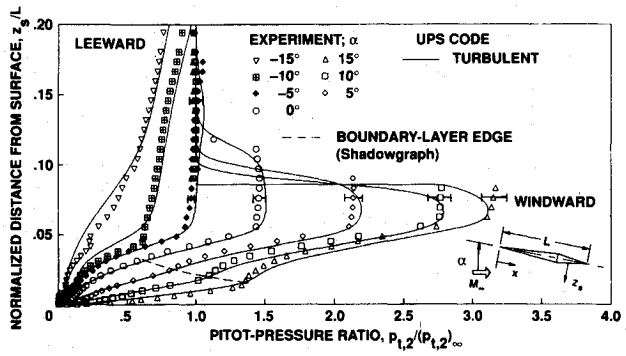

a) Entire shock layer

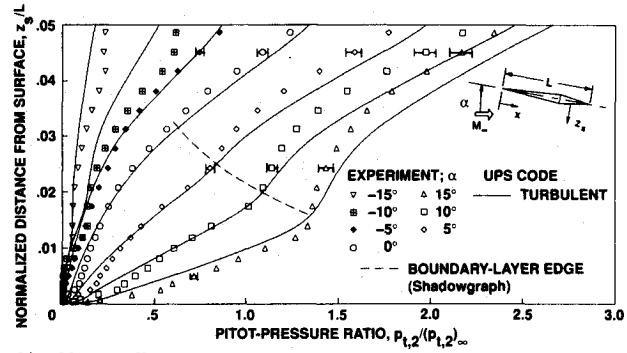

b) Near wall

Fig. 18 Effect of angle of attack on pitot-pressure distributions at $x/L = 0.8$ for model centerline: $M_\infty = 7.4$; $Re_{\infty,L} = 15 \times 10^6$; $H_w/H_t = 0.4$.

Comparisons of the experimental pitot pressures on centerline at $\alpha = 0$ deg with computational solutions from the UPS code are given in Fig. 17 at various afterbody stations. Results are given for the entire shock layer and, with expanded coordinate scales, near the wall to more clearly show details of the boundary layer. The boundary-layer edge indicated in the figures was estimated from shadowgraphs of the flow. Generally good agreement is demonstrated by the comparisons for the shock layer except near the bow wave, which is not sharply defined by these computations due to the coarseness of the grid used in the outer flow. Planned use of adaptive grids with the UPS code should help resolve the flow near the bow wave. The experimental and UPS code results agree well in the outer part of the boundary layer, whereas the UPS code underpredicts the experimental results near the wall.

Experimental pitot-pressure profiles of the shock layer are compared with solutions by the UPS code in Fig. 18 for an angle-of-attack range of -15 deg (leeward) to 15 deg (windward). Comparisons are made on the model centerline at $x/L = 0.8$ for the entire shock layer and, with expanded coordinate scales, near the wall to more clearly show details of the boundary layer and the merging of the boundary layer with the expansion region of the flow for $\alpha \geq 0$ deg. The boundary-layer edge was again estimated from shadowgraphs of the flow. The UPS code results are considered in good agreement overall with experiment except near the bow wave because of grid resolution, as previously discussed for Fig. 17. On the windward side ($\alpha \geq 0$ deg), the merging of the viscous and expansion regions of the flow are predicted well by the code. The abrupt change in pitot pressure at the edge of the boundary layer for the higher angles of attack is predicted. At $\alpha = 0$ deg, both the experimental and UPS code results indicate a smooth transition from the viscous region into the expansion region. Leeward for $\alpha = -10$ and -15 deg, small differences can be seen for the expansion region, but good agreement is shown in the outer regions of the shock layer.

Concluding Remarks

This paper described a comprehensive test program conducted in the NASA Ames 3.5-ft Hypersonic Wind Tunnel for obtaining data on a generic all-body hypersonic vehicle for CFD code validation and/or calibration, outlined the basic features of the UPS code (an upwind parabolized Navier-Stokes solver) currently being applied to the all-body model, and presented experimental and computational results on flow visualization (shadowgraphs and oil-flow patterns), surface pressures, surface heat transfer, and pitot-pressure flowfield surveys for the sharp-nosed model at a freestream Mach number of 7.4 and angles of attack from 0 to 15 deg. The results indicated significant changes from the forebody (conical) to the afterbody (nonconical) flows. Complex leeward flow was observed at angle of attack with crossflow separation and vortices. There was generally good agreement between the experimental and UPS code results for shock-wave angles, surface pressures (some differences at higher angles of attack and near leading edge), surface heat transfer (some differences for afterbody and leeward flows), and afterbody pitot-pressure surveys (some differences for leeward flow at higher angles of attack and inner region of viscous layer). The data from this study are invaluable for the validation and/or calibration of not only the UPS code, but for other codes being developed at NASA Ames and other organizations.

References

[1]Penaranda, F. E., and Freda, M. S. (eds.), "Aeronautical Facilities Catalogue, Volume I, Wind Tunnels," NASA RP-1132, Jan. 1985.

[2]Gregory, T. J., Wilcox, D. E., and Williams, L. J., "The Effects of Propulsion System-Airframe Interactions on the Performance of Hypersonic Aircraft," AIAA Paper 67-493, July 1967.

[3]Gregory, T. J., Williams, L. J., and Wilcox, D. E., "The Air-breathing Launch Vehicle for Earth Orbit Shuttle—Performance and Operation," AIAA Paper 70-270, Feb. 1970.

[4]Gregory, T. J., Ardema, M. D., and Waters, M. H., "Hypersonic Transport Preliminary Performance Estimates for an All-Body Configuration," AIAA Paper 70-1224, Oct. 1970.

[5]Williams, L. J., "Estimated Aerodynamics of All-Body Hypersonic Aircraft Configurations," NASA TM X-2091, March 1971.

[6]Nelms, W. P., Jr., and Thomas, C. L., "Aerodynamic Characteristics of an All-Body Hypersonic Aircraft Configuration at Mach Numbers from 0.65 to 10.6," NASA TN D-6577, Nov. 1971.

[7]NACA Ames Research Staff, "Equations, Tables, and Charts for Compressible Flow," NACA Rept. 1135, 1953.

[8]Bertram, M. H., "Comment on 'Viscosity of Air'," *Journal of Spacecraft and Rockets,* Vol. 4, No. 2, 1967, pp. 287–288.

[9]Maltby, R. L., "Flow Visualization in Wind Tunnels Using Indicators," AGARDograph 70, April 1962, pp. 1–74.

[10]Foster, T. F., and Lockman, W. K., "Results of Heat Transfer Tests of an 0.0175-Scale Space Shuttle Vehicle Model 22-OTS in the NASA-Ames 3.5-Foot Hypersonic Wind Tunnel," NASA CR-141, 514, April 1975.

[11]Lawrence, S. L., Chaussee, D. S., and Tannehill, J. C., "Application of an Upwind Algorithm to the Three-Dimensional Parabolized Navier-Stokes Equations," AIAA Paper 87-1112, June 1987.

[12]Baldwin, B. S., and Lomax, H., "Thin-Layer Approximation and Algebraic Model for Separated Turbulent Flows," AIAA Paper 78-257, Jan. 1978.

[13]Degani, D., and Schiff, L. B., "Computation of Supersonic Viscous Flows Around Pointed Bodies at Large Incidence," AIAA Paper 83-0034, Jan. 1983.

[14]Srinivasan, S., Tannehill, J. C., and Weilmuenster, K. J., "Simplified Curve Fits for the Thermodynamic Properties of Equilibrium Air," NASA RP 1181, Aug. 1987.

[15]Buelow, P. E., Tannehill, J. C., Ievalts, J. O., and Lawrence, S. L., "Three-Dimensional Upwind Parabolized Navier-Stokes Code for Chemically Reacting Flows," AIAA Paper 90-0394, Jan. 1990.

[16]Hayes, W. D., and Probstein, R. F., *Hypersonic Flow Theory,* 1st ed., Academic, New York, 1959, pp. 277–281.

[17]Cleary, J. W., "Approximation for Distribution of Flow Properties in the Angle-of-Attack Plane of Conical Flows," NASA TN D-5951, Aug. 1970.

[18]Fay, J. A., and Riddell, F. R., "Theory of Stagnation Point Heat Transfer in Dissociated Air," *Journal of Aeronautical Sciences,* Vol. 25, No. 2, 1958, pp. 73–85, 121.

Gerald T. Chrusciel
Associate Editor